Numerical Evaluation of Noise Sources and Statistics from High-Speed Two-Phase Jet Flow

Wei Wang,* S. Balachandar,† and Steven A. E. Miller‡
University of Florida, Gainesville, FL 32611

Understanding sound generation from high-speed particle-laden jets is important for designing propulsion systems in the aerospace industry. We present a numerical method to evaluate the flow-field, far-field noise, and equivalent noise sources in a Mach 1.5 particle-laden jet. The method consists of numerically solving compressible Navier-Stokes equations, tracking each particle in the Lagrangian reference frame, solving Ffowcs Williams and Hawking's equation, and evaluating equivalent sound sources using various acoustic analogies. We compare flow-field, sound sources, and far-field sound spectra in the downstream direction from a gas and particle-laden jet at the same nozzle pressure ratio and total temperature ratio. The sound sources are greatly altered by the particles. Moreover, we directly evaluate the monopole and dipole sources due to the presence of particles in the particle-laden jet using Crighton and Ffowcs William's acoustic analogy. These two sources are directly related to the particles volume fraction and aerodynamic force applied by the particles to the gas. They are orders of magnitude smaller than the sound sources due to the turbulence. The monopole sources are more correlated, while dipole sources are very compact in space. Both sources convect at a subsonic speed, which is comparable to the local particles' velocity.

Nomenclature

Symbols

c	local speed of sound
$c_{p,p}$	specific heat of the particle
c_∞	ambient speed of sound
D	nozzle exit diameter
d_p	diameter of the particle
E	total energy
E_p	energy source from particles
$\boldsymbol{F}_c$	convective flux vector
$\boldsymbol{F}_v$	viscous flux vector
$f_{e,i}$	external volumetric forces
$f_{p,i}$	momentum source from particles
$g(x,t)$	function representing FWH surface
$\mathcal{G}_{ij}$	Goldstein's source term
H	total enthalpy
$\mathcal{H}(x)$	Heaviside function
k	thermal conductivity
ℓ_i	local force on the FWH surface
m_p	mass source of particles
$\boldsymbol{n}$	face normal vector
$\boldsymbol{n'}$	face normal vector from FWH surface
p	pressure
p'	pressure fluctuations
p_∞	ambient static pressure
$\boldsymbol{Q}$	source term vector
$\dot{q}_h$	external heat source
R	gas constant
$\boldsymbol{r}$	vector from FWH surface to observer position
S_{ij}	strain rate tensor
T	temperature
T_∞	ambient static temperature
T_p	temperature of particle
$\mathcal{T}_{ij}$	Lighthill's stress tensor
t	time
$\boldsymbol{\mathcal{U}}$	FWH surface velocity vector
u_j	fully-expanded jet velocity
$\boldsymbol{V}$	velocity vector
V_n	face normal velocity
$\boldsymbol{V}_p$	velocity vector of the particle
$\boldsymbol{\mathcal{V}}$	FWH surface flow velocity vector
$\boldsymbol{W}$	conservative variable vector
$\boldsymbol{x}_p$	particle position vector

Greek Symbols

δ_{ij}	Kronecker delta
$\delta(x)$	Dirac delta function
θ	radiation angle from upstream nozzle axis
μ	dynamic viscosity
ν	kinematic viscosity
ρ	density
ρ_p	density of the particle
ρ'	density fluctuations
ρ_∞	ambient density
σ_{ij}	viscous stress tensor
τ	retarded time
τ_{ij}	shear stress tensor
τ^u	particle response time
τ^θ	thermal response time
Ω	control volume
$d\Omega$	control surface

Non-Dimensional Numbers

M_d	design Mach number of nozzle

*Ph.D. Candidate, Department of Mechanical and Aerospace Engineering, University of Florida, P.O. Box 116250, Gainesville, FL 32611, USA, AIAA Student Member, wei.wang@ufl.edu; wangwei.nick@gmail.com

†Distinguished Professor, Department of Mechanical and Aerospace Engineering, University of Florida, P.O. Box 116250, Gainesville, FL 32611, USA, AIAA Senior Member, bala1s@ufl.edu

‡Assistant Professor, Department of Mechanical and Aerospace Engineering, University of Florida, P.O. Box 116250, Gainesville, FL 32611, USA, AIAA Lifetime / Senior Member, saem@ufl.edu; saemiller@gmail.com

M_j	fully-expanded Mach number
M_∞	free-stream Mach number
$\boldsymbol{M}$	Mach number of FWH surface velocity vector
$\mathcal{M}$	Mach number of flow velocity vector
Pr	Prandtl number
Re_p	particle Reynold's number
St	Strouhal number

Abbreviations

BBSAN	broadband shock-associated noise
CFD	computational fluid dynamics
FWH	Ffowcs Williams Hawkings
LES	large-eddy simulation
NPR	nozzle pressure ratio
PIV	particle image velocimetry
SPL	sound pressure level
TKE	turbulent kinetic energy
TTR	total temperature ratio

I. Introduction

High-speed two-phase air particle jet flows commonly appear in propulsion systems that use solid propellant in the aerospace industry and military applications. The high specific impulse of solid propellant often is ideal for accelerating the space vehicle through the launch and initial ascent stage [1]. Two-phase jet flows radiate and propagate unique sound waves that are different than the noise generated from single-phase jets. Furthermore, the sound characteristics and generation mechanisms associated with multiphase jets are not well understood. The existence of the solid particles alters the turbulence, shock-waves, and acoustic radiation [2]. The intense acoustic radiation from the jet flow can cause sonic fatigue and even failure of the launch vehicle [3], and are considered an environmental impact or even hazard [4, 5]. These issues require the community to investigate and understand multiphase jet flow and its acoustics sources. There are few studies on solid rocket noise prediction. But most of the studies are based on semi-empirical methods and they usually do not distinguish between single-phase and multiphase jet flow. Publicly available studies on two-phase jet aeroacoustics are very limited, and the noise reduction methods for solid rockets are not fully studied by the community. Here, we combine advances in multiphase computational fluid dynamics (CFD) with advanced analysis of acoustic analogy theory to understand the differences of the noise sources.

Previous Approaches

Here, we summarize previous approaches, but our review is not exhaustive. For a full review of the subject see McInerny [6, 7], Bourgine and Dordain [8] of ONERA, Humphrey [9], and Regier et al. [10]. Over the past few decades, many researchers have attempted to measure and predict the noise from rockets. Direct measurement of the acoustic environment at launch of a rocket often provides valuable information for future study. Therefore, launch programs conduct noise measurements. Publicly available reports are available since the 1950s. Cole et al. [11] gathered near- and far-field noise measurements of 14 types of rockets, and compared noise characteristics of these launches to study the impact of using different flame deflectors [12]. They also reported noise measured from Saturn SA-1 launches [13], and 23 rocket/missile launches at Cape Canaveral Missile Test Annex [14]. Sutherland [15] reported on the acoustic and vibration environment of Saturn S-IB launches. Tedrick and Thornton [16] recorded far-field noise of SA-4 and Titan launches [17]. Alestra et al. [18] analyzed and located the sound source of an ARIANE 5 rocket launch using an inverse method. Panda et al. [19] recorded noise of the Antares vehicle launch and measured the noise source with a microphone phase array. All these studies provided valuable experimental data for the community to facilitate the understanding of noise from rockets.

Static firings of rocket engines also provides valuable data, but in a more controllable way than during launch. The most common measurements of the static firing of a rocket are the near- and far-field acoustic pressure. Such studies, from Lassiter and Heikotter [20], Mull and Erickson [21], Mayes et al. [22], Tedrick [23], Foulon et al. [24], Fukuda et al. [25], and Horne et al. [26] are valuable for the purpose of validating the design of a specific model of rocket or empirical relation. But empirical models do not provide information on the flow-field due to the limitation of the instruments, therefore they are not suitable for identifying the sound sources. Source localization techniques, such as microphone phased arrays and beamforming, are used in static firing of rockets to find the sound source. A series of studies conducted by Panda and Mosher [27–29] used an array of 70 microphones and the beamforming technique to locate the noise source within the exhaust of different rockets. Gely et al. [30] and Casalino et al. [31] also measured the acoustic environment of a mock-up model of the VEGA launch vehicle with microphone array. But these beamforming techniques assumed the sound waves are strictly linear and travel at constant velocity, which is overly simplied for the rocket plume. Moran and Houston [32] employed infrared imagery for measuring and visualization of the static firing test of solid rocket motors. Although these techniques provided more information, directly measuring the rocket flow-field, such as density, pressure and velocity, is still not feasible as of now. A feasible way of studying the flow-field of a solid rocket is to simulate the jet flow in a wind-tunnel environment. Panda et al. [33, 34] conducted a wind-tunnel

test to simulate solid-rocket plumes from the abort motor using high-pressure helium gas. Unfortunately, wind-tunnel tests cannot provide information on solid particles interacting with the jet flow.

As the capability of super computing increased, numerical simulation became a more important tool to investigate the noise. Numerical simulations can provide detailed flow quantities that are difficult to measure for rockets. The most well known approach is of Kiris et al. [35] who as a group at NASA Ames developed the Launch Ascent and Vehicle Aerodynamics (LAVA) CFD solver. Another approach is the Loci/CHEM code, which is capable of simulating two-phase flows using an Euler-Lagrangian approach. Loci/CHEM is validated with the Ares I Scale Model Acoustics Test (ASMAT) by Putnam and Strutzenburg [36, 37] and was applied to evaluate the water spary system "rainbird" at the Kennedy Space Center by Putnam [38, 39]. Buchta et al. [40] direct simulated the sound in the near-field of a compressible free-shear flow with particulates. Hybrid methods utilizing LES and the acoustic analogy are perhaps the most promising tools for prediction of the far-field acoustic pressure of rockets. Fukuda et al. [25] predicted pressure using a hybrid implicit LES / Kirchhoff method and validated it with measurement of static firing of a solid rocket.

Empirical relations have been widely used in the community for predicting rocket noise and designing new space vehicles. But they are only accurate for specific rocket and launch pad configurations, and, more importantly, they provide little insight into the physics of the noise generation processes. Chobotov and Powell [41] presented an empirical approach for the far-field noise from rockets based on the observation that the total acoustic power is a fraction of total mechanical power. Franken [42] also created empirical models to identify noise sources, source propagation, and the structural response on the flight vehicle. Morgan et al. [43] discussed the feasibility of using an acoustic scaled model for near-field noise. Wilhold et al. [44] presented an empirical equation for the noise level using the "sound-source motion;" the engine parameters including thrust, flow rate, gas exit velocity, and number of engines; the sound energy loss due to molecular absorption; and a distribution factor. Crocker and Potter [45] extensively reviewed and tested empirical models based on curve fitting, and produced a prediction method based on the assumption that spectral components of acoustic sources are distributed spatially within the plume. Eldred [46] reviewed a large number of prediction methods of rocket noise and proposed a "best fit" approach of predicting noise using empirical curves. Candel [47] investigated the radiating sound field from rockets using a semi-empirical model that is based on dimensional analysis, and showed good agreement with noise measured at Ariane rocket launches. Casalino et al. [48] proposed and validated a modified empirical model for rocket noise. Fukuda et al. [25] compared the empirical relation, NASA SP-8072, and measurement from a solid rocket and over-predicted the noise in the downstream direction.

Reduction of noise at launch and lift-off have been partially accomplished by injecting water on the launch pad or within the flame deflector. Examples include Cole et al. [12], who investigated directing rocket exhaust into water tanks, Counter and Houston [49] from the Ares I Scale Model Acoustic Test (ASMAT) program, Foulon et al. [24], Gely et al. [50] from the Ariane 5 program, and Ignatius et al. [51]. Although some success in reduction of noise was found, future reduction methods require greater understanding of the aerodynamics of the rocket plume and its relation with the radiated noise.

Present Approach

Previous efforts have focused entirely on measurement, creating empirical models from measurement, or performing numerical simulations on supercomputers. We overcome previous limitations by combining contemporary acoustic analogy theory with simplified numerical simulations. Moreover, we pay special attention to the impact of the two-phase process for the far-field acoustics, which is not actively studied nor well-understood by the community. We know that the particles and/or droplets in the exhaust from the burning process of solid propellant [52] actively alters the turbulent structures and energy cascade [53]. The presence of particles also alters the propagation characteristics of sound waves. Therefore, it is very important to discover the role of particulates in the noise generation process and to expand aeroacoustic theory, which was developed for single-phase jets. In this paper, we mainly examine the changes of turbulence and sound sources due to the particulates in the flow. Furthermore, we focus on evaluating and assessing the noise radiated from large-scale turbulent structures.

In the next section, we present our numerical method to predict the flow-field of the rocket exhaust with and without particles. The Ffowcs Williams and Hawkings (FWH) method and its implementation are then discussed. We perform a numerical simulation and far-field noise calculation for single phase and two-phase gas-particle jet flows under the same condition. Aerodynamic and aeroacoustic statistics of single phase jets are validated with experimental results. The impact of aluminum particulates on both the turbulent statistics and far-field sound spectra are studied by comparing the flow with and without particles. Comparisons of the mean flow, turbulence, and acoustic statistics of single phase and particle-laden jet flows are shown in the results section. We choose to evaluate the sound source using Lighthill's

acoustic analogy [54] and Goldstein's generalized acoustic analogy [55] with the base flow being the mean flow. We compare the mean, variance, skewness, and kurtosis of the most prominent component of the chosen source term of single and two-phase jets. We also compare the two-point cross-correlation of the sound source with and without particulates. Finally, we summarize our present effort and draw the main conclusions.

II. Methodology

Computational Approach

The prediction of the far-field noise from the jet exhaust is performed in two stages. In the first stage, an implicit LES simulation is conducted for different jet conditions. We adopt a two-way coupled Eulerian-Lagrangian approach to simulate the particle-gas two-phase flow at the same nozzle pressure ratio (NPR). In other words, the ratio of total pressure to the ambient pressure are the same. The continuous phase, air, is treated with an Eulerian framework, while aluminum particles are tracked using a Lagrangian mode. These particles alter the carrier phase by coupling with the momentum and energy equations. They continuously exchange momentum and energy with the gas phase through the relaxation processes. Field-variables are sampled every 10^{-5} seconds on an encompassing porous acoustic surface and are subsequently used as input to the acoustic solver. The acoustic solver, which is described later, is based on the FWH equation and calculates the far-field fluctuating acoustic pressure. The sound pressure level (SPL) is derived using signal processing of the acoustic pressure. In the next section, we present the governing equations for the gas phase, particulates, and acoustics.

Gas Phase

We model the multiphase rocket exhaust using the filtered Navier-Stokes equations with additional terms for particulates [56]. The equations are written in integral-vector form as

$$\frac{\partial}{\partial t}\int_{\Omega} \boldsymbol{W}\, d\Omega + \oint_{\partial\Omega} \boldsymbol{F_c}\, dS = \oint_{\partial\Omega} \boldsymbol{F_v}\, dS + \int_{\Omega} \boldsymbol{Q} d\Omega, \tag{1}$$

where $\boldsymbol{F}_c$ is a vector of convective fluxes, $\boldsymbol{F}_v$ is a vector of viscous fluxes, $\boldsymbol{Q}$ is a vector source term, t is time, $\boldsymbol{W}$ is a vector of conservative variables, Ω represents volumetric integration, and $\partial\Omega$ represents a flux integral. The vectors $\boldsymbol{W}$, $\boldsymbol{F}_c$, and $\boldsymbol{F}_v$ are

$$\boldsymbol{W} = \left[\rho, \rho u, \rho v, \rho w, \rho E\right]^T, \tag{2}$$

$$\boldsymbol{F_c} = \left[\rho V_n, \rho u V_n + n_x p, \rho v V_n + n_y p, \rho w V_n + n_z p, \rho H V_n\right]^T, \tag{3}$$

and

$$\boldsymbol{F_v} = \begin{bmatrix} 0 \\ n_x\tau_{xx} + n_y\tau_{xy} + n_z\tau_{xz} \\ n_x\tau_{yx} + n_y\tau_{yy} + n_z\tau_{yz} \\ n_x\tau_{zx} + n_y\tau_{zy} + n_z\tau_{zz} \\ n_x\Theta_x + n_y\Theta_y + n_z\Theta_z \end{bmatrix}. \tag{4}$$

Here, E is total energy, H is total enthalpy, and the face normal velocity is $V_n = n_x u + n_y v + n_z w$, where $\boldsymbol{n} = [n_x, n_y, n_z]^T$ is the face normal vector. The shear stress tensor is defined as $\tau_{ij} = 2\mu S_{ij} - \frac{2}{3}\mu\frac{\partial u_k}{\partial x_k}\delta_{ij}$, where $S_{ij} = \frac{1}{2}(\partial u_i/\partial x_j + \partial u_j/\partial x_i)$ is the strain rate tensor and μ is dynamic viscosity. Dynamic viscosity is computed from Sutherland's law, $\mu = \mu_{ref}(TT_{ref}^{-1})^{3/2}(T_{ref} + S)(T + S)^{-1}$, where $\mu_{ref} = 1.716 \times 10^{-5}$ kgm^{-1}s^{-1}, $T_{ref} = 273.15$ K, $S = 110.4$ K, and δ_{ij} is the Kronecker delta function. The vector $\boldsymbol{\Theta}$ is

$$\begin{aligned}\Theta_x &= u\tau_{xx} + v\tau_{xy} + w\tau_{xz} + k\frac{\partial T}{\partial x},\\ \Theta_y &= u\tau_{yx} + v\tau_{yy} + w\tau_{yz} + k\frac{\partial T}{\partial y},\\ \Theta_z &= u\tau_{zx} + v\tau_{zy} + w\tau_{zz} + k\frac{\partial T}{\partial z},\end{aligned} \tag{5}$$

where k is the thermal conductivity and T is the temperature. This term represents the work of the viscosity and heat conduction. Finally, the vector $\boldsymbol{Q}$ is

$$\boldsymbol{Q} = \begin{bmatrix} m_p \\ \rho f_{e,x} + f_{p,x} \\ \rho f_{e,y} + f_{p,y} \\ \rho f_{e,z} + f_{p,z} \\ \dot{q}_h + E_p \end{bmatrix}, \tag{6}$$

where E_p is the energy source from particles, $f_{e,i}$ are external volumetric forces, $f_{p,i}$ are momentum sources from particles, m_p is the mass source of particles, and $\dot{q}_h$ is the external heat source. The vector $\boldsymbol{Q}$ represents additional body forces and forces due to the particulates within the flow.

Pressure, temperature, and density are related through the ideal gas law

$$p = \rho RT, \tag{7}$$

where R is the gas constant.

Lagrangian Particles

The evolution equations for position, velocity, and temperature of a single Lagrangian particle are

$$\frac{d}{dt}\boldsymbol{x}_p = \boldsymbol{V}_p, \tag{8}$$

$$\frac{d}{dt}\boldsymbol{V}_p = \frac{\boldsymbol{V} - \boldsymbol{V}_p}{\tau^u}, \tag{9}$$

and

$$\frac{d}{dt}T_p = \frac{T - T_p}{\tau^\theta}, \tag{10}$$

where $\boldsymbol{x}_p = \left\{x_p, y_p, z_p\right\}^T$ is the position vector of the particle, $\boldsymbol{V} = \left\{u_p, v_p, w_p\right\}^T$ is the velocity vector of the gas at the particle position, $\boldsymbol{V}_p$ is the velocity vector of the particle, and T and T_p are the temperature of the gas phase at the particle position and the temperature of the particle, respectively.

The particle response and thermal response times are modeled as

$$\tau^u = \frac{\rho_p d_p^2}{18\mu f_u(Re_p)} \tag{11}$$

and

$$\tau^\theta = \frac{c_{p,p}\rho_p d_p^2}{12k f_\theta(Re_p)}, \tag{12}$$

where $c_{p,p}$ is the specific heat of the particle, d_p is the diameter of the particle, ρ_p is the density of the particle, and μ is the dynamic viscosity of the gas phase evaluated at the particle position. Since Re_p is typically larger than unity, we use the following correlation [57] for Stokes' drag

$$f_u(Re_p) = 1 + 0.15Re_p^{0.687} \tag{13}$$

and the Ranz-Marshall correlation [58] for energy

$$f_\theta(Re_p) = 1 + 0.3Re_p^{1/2}Pr^{1/3}, \tag{14}$$

where the particle Reynold number is

$$Re_p = \frac{d_p|\boldsymbol{V} - \boldsymbol{V}_p|}{\nu}. \tag{15}$$

Here, ν is the kinematic viscosity of gas at the particle position. Forces exerted by particles on the fluid are

$$\boldsymbol{f}_p = -\sum \frac{\pi d_p^3 \rho_p}{6\tau^u}(\boldsymbol{V}_p - \boldsymbol{V}), \tag{16}$$

where $\sum$ denotes summation over all the particles within the finite volume cell. Energy transfer from each individual particle to the surrounding fluid is governed by

$$E_p = \sum \left[\boldsymbol{f}_p \cdot (\boldsymbol{V}_p - \boldsymbol{V}) - \frac{\pi d_p^3 \rho_p c_{p,p}}{6\tau^\theta}(T_p - T) \right]. \tag{17}$$

Ffowcs Williams Hawking's Equation

Lighthill [54] derived the acoustic analogy by rearranging the Navier-Stokes equations into an inhomogeneous wave equation with an equivalent source term. Ffowcs Williams and Hawkings [59] used generalized functions and included the effects of surfaces in arbitrary motion in the context of the wave equation. The FWH equation as originally proposed is

$$\left(\frac{1}{c^2}\frac{\partial^2}{\partial t^2} - \frac{\partial^2}{\partial x_i^2}\right) p' = \frac{\partial}{\partial t}\left[\rho_\infty \mathcal{U}_{n'}\right]\delta(g) - \frac{\partial}{\partial x_i}\left[p n_i' \delta(g)\right] + \frac{\partial^2}{\partial x_i \partial x_j}\left[\mathcal{T}_{ij}\mathcal{H}(g)\right], \tag{18}$$

and for a penetrable porous surface is

$$\left(\frac{1}{c^2}\frac{\partial^2}{\partial t^2} - \frac{\partial^2}{\partial x_i^2}\right) p' = \frac{\partial}{\partial t}\left[\rho_\infty U_{n'}\right]\delta(g) - \frac{\partial}{\partial x_i}\left[L_i \delta(g)\right] + \frac{\partial^2}{\partial x_i \partial x_j}\left[\mathcal{T}_{ij}\mathcal{H}(g)\right], \tag{19}$$

where $U_{n'} = (1 - \rho\rho_\infty^{-1})\mathcal{U}_{n'} + \rho\mathcal{V}_{n'}\rho_\infty^{-1}$, $L_i = p\delta_{ij}n_j' + \rho\mathcal{V}_i(\mathcal{V}_{n'} - \mathcal{U}_{n'})$, and $\mathcal{T}_{ij} = \rho\mathcal{V}_i\mathcal{V}_j - \sigma_{ij} + (p' - c_\infty^2\rho')\delta_{ij}$. Note that $\mathcal{T}_{ij}$ is the Lighthill stress tensor, σ_{ij} is the viscous stress tensor, $\mathcal{H}(g)$ is the Heaviside function, and δ is the Dirac delta function. The first and second term on the right hand side of Eqns. (18) and (19) represents the acoustic monopole and dipole source terms on the porous surface, while the last term represents the acoustic quadrupole source terms in the volume surrounding the body.

The FWH surface is defined by an equation of the form $g(x,t) = 0$ subject to $\nabla \boldsymbol{g} = \boldsymbol{n'}$, where $\boldsymbol{g}$ is a space and time function representing the surface and $\boldsymbol{n'}$ is the unit outward normal to the surface. We assume p' is acoustic pressure when the fluctuations in density are very small compared to the ambient density (i.e. $\rho'\rho_\infty^{-1} << 1$). The acoustic pressure is $p' = c_\infty^2\rho' = c_\infty^2(\rho - \rho_\infty)$, where c_∞ is the ambient speed of sound. The variables p, $\boldsymbol{\mathcal{V}}$, and $\boldsymbol{\mathcal{U}}$ are the local static pressure, the flow velocity, and the velocity with which the surface moves, respectively.

Farassat's Solution of FWH Equation

Farassat [60] derived his Formulation 1A from Eqn. (18) to predict pressure in the far-field from the FWH surface when the flow velocity is zero. We position a FWH surface plane, which represent the porous surfaces, within the flow-field that encloses the turbulence of the jet plume. The velocity fluctuations are non-zero on the porous surface. We follow the formulation of Farassat [60] and derive additional source terms that contain velocity fluctuations. We find

$$
\begin{aligned}
4\pi p'(x,t) = \int_{-\infty}^{\infty} \Bigg[& \frac{\rho_\infty \dot{\mathcal{U}}_{n'}}{r(1-M_r)^2} + \frac{\rho_\infty \mathcal{U}_{n'}(r\dot{M}_r + c(M_r - M^2))}{r^2(1-M_r)^3} + \frac{\dot{\ell}_r}{cr(1-M_r)^2} + \frac{\ell_r - \ell_i \cdot M_i}{r^2(1-M_r)^2} \\
& + \frac{\ell_r(r\dot{M}_r + c(M_r - M^2))}{cr^2(1-M_r)^3} + \left(\frac{\dot{\rho}(\mathcal{V}_{n'} - \mathcal{U}_{n'}) + \rho(\dot{\mathcal{V}}_{n'} - \dot{\mathcal{U}}_{n'})}{r(1-M_r)^2} \right)(1 + \mathcal{M}_r) + \frac{\rho(\mathcal{V}_{n'} - \mathcal{U}_{n'})}{r(1-M_r)^2}\dot{\mathcal{M}}_r \\
& + \frac{\rho(\mathcal{V}_{n'} - \mathcal{U}_{n'})(\mathcal{V}_r - \mathcal{V}_i M_i)}{r^2(1-M_r)^2} + \frac{\rho(\mathcal{V}_{n'} - \mathcal{U}_{n'})(1 + \mathcal{M}_r)}{r^2(1-M_r)^3}(r\dot{M}_r + c(M_r - M^2)) \Bigg]_{ret} dS,
\end{aligned} \tag{20}
$$

where $r = |\boldsymbol{x} - \boldsymbol{y}|$ is the distance from each location of the porous surface $\boldsymbol{y}$ to the observer location $\boldsymbol{x}$. $\boldsymbol{M}$ and $\boldsymbol{\mathcal{M}}$ denote the Mach number of the surface velocity and flow velocity, respectively with components $M_i = \mathcal{U}_i c_\infty^{-1}$ and $\mathcal{M}_i = \mathcal{V}_i c_\infty^{-1}$. The variable $\ell_i = p \cdot n_i'$ is the component of the local force intensity that acts on the fluid. A dot over the variable represents the time derivative. The subscript $\boldsymbol{r}$ denotes the dot product for any given quantity with the unit radiation vector. The subscript ret means that the quantities inside the bracket are evaluated at the retarded time. The area of each face on the FWH surface is denoted by dS.

We elect to keep the FWH surface stationary relative to the nozzle. Hence, we can substitute $\boldsymbol{\mathcal{U}} = 0$ and $\boldsymbol{M} = 0$ into Eqn. (20) and simplify

$$
4\pi p'(x,t) = \int_{-\infty}^{\infty} \left[\frac{\dot{\ell}_r}{cr} + \frac{\ell_r}{r^2} + \left(\frac{\dot{\rho}\mathcal{V}_{n'} + \rho\dot{\mathcal{V}}_{n'}}{r} \right)(1 + \mathcal{M}_r) + \frac{\rho\mathcal{V}_{n'}}{r}\dot{\mathcal{M}}_r + \frac{\rho\mathcal{V}_{n'}\mathcal{V}_r}{r^2} \right]_{ret} dS. \tag{21}
$$

Crighton and Ffowcs Williams Acoustic Analogy

Crighton and Ffowcs Williams [61] investigated the sound sources in two-phase flows using exact rearrangement of volume averaged Navier-Stokes equations of two-phase flow,

$$
\begin{aligned}
\frac{\partial}{\partial t}\rho + \frac{\partial}{\partial x_j}\rho V_j &= Q, \\
\frac{\partial}{\partial t}\rho V_i + \frac{\partial}{\partial x_j}\left[(1-\alpha)\rho V_i V_j + p_{ij}\right] &= G_i.
\end{aligned} \tag{22}
$$

Here α is the local volume fraction of the particles, and the equivalent sources are

$$
\begin{aligned}
Q &= -\rho\left(\frac{\partial}{\partial t} + V_j\frac{\partial}{\partial x_j}\right) ln(1-\alpha), \\
G_i &= F_i + \frac{\partial}{\partial t}\alpha\rho V_i.
\end{aligned} \tag{23}
$$

The Crighton and Ffowcs William (C-FW) acoustic analogy is

$$
\left(\frac{\partial^2}{\partial t^2} + c_\infty^2\nabla^2\right)\rho = \frac{\partial Q}{\partial t} - \frac{\partial G_i}{\partial x_i} + \frac{\partial^2 T_{ij}}{\partial x_i x_j}. \tag{24}
$$

Comparison with Lighthill's analogy [54] shows that extra monopole and dipole sources arise from the effect of particles. Equation 23 shows the source of Q and G_i are indeed caused by the nonuniform distribution of particles or the time rate change of volume fraction α. The location, convection, and statistics of sound sources are analyzed in the results and discussion section.

III. Results and Discussion

Problem Overview

Figure 1 shows the geometry of the flow domain and computational grid used for the numerical study. We include the nozzle geometry in our computation. This allows us to capture the flow and particles interacting with the nozzle wall,

which are essential for the development of the boundary layer inside the nozzle and shear layer from the nozzle exit. The geometry is based on the "SMC016" nozzle obtained from the Small Hot Jet Acoustic Rig (SHJAR) [62] experiments, for the purpose of validating our solver. The SMC016 nozzle is convergent-divergent with a design Mach number of 1.5 and exit diameter of 0.0508 m (2 inches). The profile of the nozzle internal wall is a smooth curve that is designed with the method of characteristic. As a result, the reflection of the Prandtl-Meyer expansion waves are canceled within the divergent section, and should generate, if any, only very weak shocks at the on-design flow condition. The total length of the nozzle is 0.25 m. The computational domain extends from the nozzle exit $50D$, or 5.08 m, in the downstream direction. It extends $4D$ in the upstream direction from the nozzle inlet and $15D$ in the cross-stream direction from the nozzle centerline.

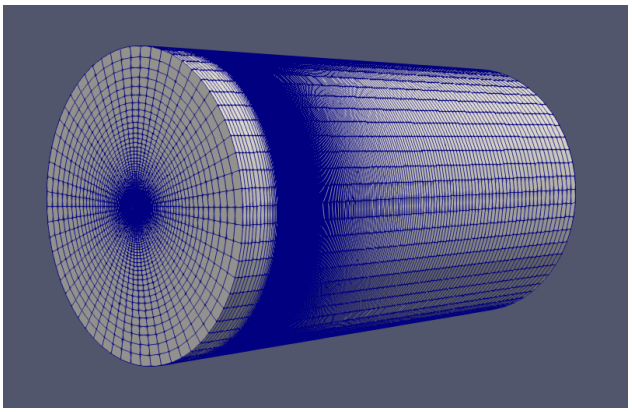

Fig. 1 Computational grid.

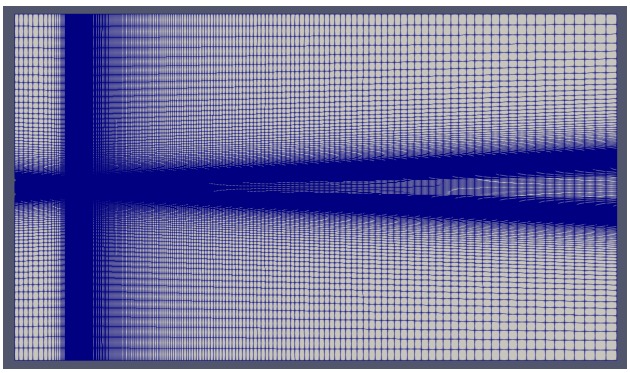

Fig. 2 Cross-section of the computational grid.

The computational grid is structured-like (note the solver is unstructured) and has 2.1 million hexahedron cells. Figure 2 shows the grid distribution along the $x - y$ plane. An O-H grid is used to avoid the singularity at the center-line of the nozzle. The minimum grid point spacing resides in the shear layer region directly downstream of the nozzle lip to capture the complex flow structures. The minimum grid point spacing is on the order of 10^{-4} m, which is equivalent to 1% of the nozzle exit diameter. The grid points are clustered within the shear layer region, the boundary layer attached on the internal nozzle wall, the nozzle exit plane, and the nozzle throat plane to acquire higher local resolution.

We initially choose to numerically simulate a cold jet with on-design flow conditions. The total temperature ratio (TTR) is 1 and the NPR is 3.67, which corresponds to a fully expanded Mach number of 1.5 for air. An ambient Mach number of 0.01 is set at the far-field boundary conditions for numerical stability. The boundary condition at the nozzle inlet prescribes the total pressure, total temperature, and the flow direction. The flow velocity, pressure, and temperature are allowed to vary at the nozzle inlet. The nozzle internal wall uses the solid wall boundary condition, where the velocity is weakly enforced to be zero through the corresponding fluxes. All the outer boundaries of the computational domain are set as far-field boundary conditions to allow sound waves to leave the domain without contaminating the solution. Solid particles are injected through the nozzle inlet at the same velocity and temperature of the local fluid. The

locations of particle injection are uniformly chosen within the boundary cells at the nozzle inlet. Therefore, the injected particles are uniformly distributed in both the streamwise and radial directions. After the particles are released into the flow, the location of individual particles are controlled by solving Eqn. (8).

Aerodynamics of the Particle-Laden Jet

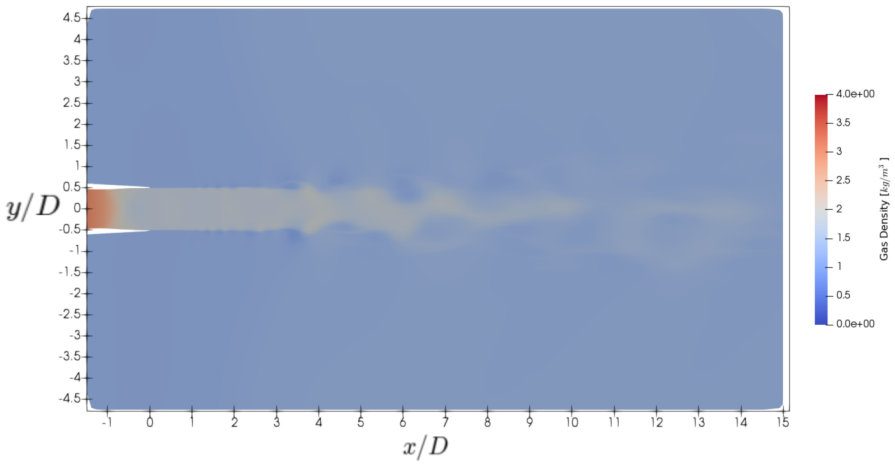

Fig. 3 Instantaneous density plot at the $x-y$ plane.

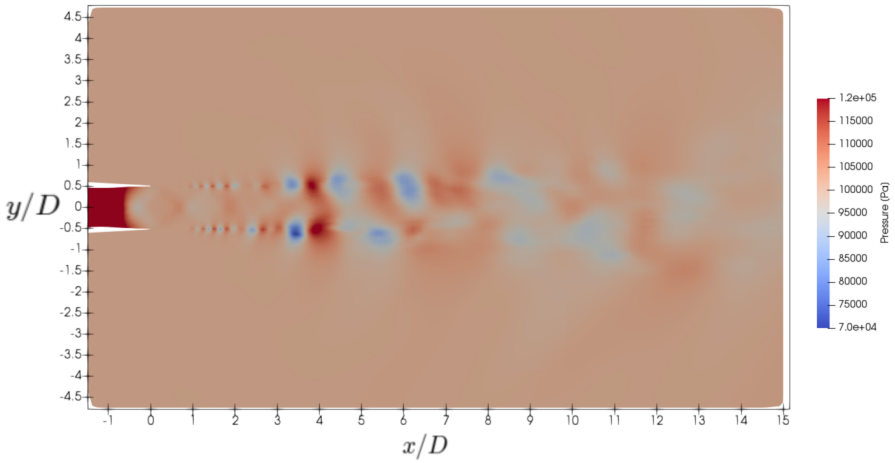

Fig. 4 Instantaneous pressure plot at the $x-y$ plane.

Figures 3 and 4 show the instantaneous density and pressure contours of the gas jet in the $x-y$ plane, respectively. It is observed that Kelvin-Helmholtz instabilities start to develop along the lipline of the nozzle within $1D$ downstream and break up further downstream close to $10D$. The potential core region ends at approximately $8D$ downstream of the nozzle exit plane. Oscillations of pressure above and below the corresponding mean pressure occur on the nozzle lipline within the exhaust. Figure 5 shows a comparison of the mean streamwise velocity on the centerline of the nozzle. The results from steady Reynolds-Averaged Navier–Stokes (RANS) simulations code called the Fully Unstructured Navier-Stokes (FUN3D) are validated with SHJAR experiments by Bridges [62]. The empirical relation is from Lau et al. [63]. It can be seen that our simulation shows good agreement with the differences less than 5 m/s up to $7.5D$, which is where the core ends. Predicted velocity of the simulation gradually reduces after $8D$ from the nozzle exit and falls-off after $20D$, while the velocity from the FUN3D solver remains almost constant until $10D$, then decreases sharply after. It is a known issue of RANS simulations that they tend to over-predict the potential core length of jet flow.

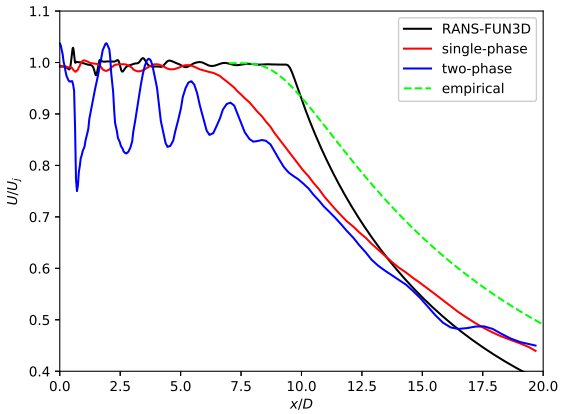

Fig. 5 Comparison of the mean velocity on the centerline of the nozzle.

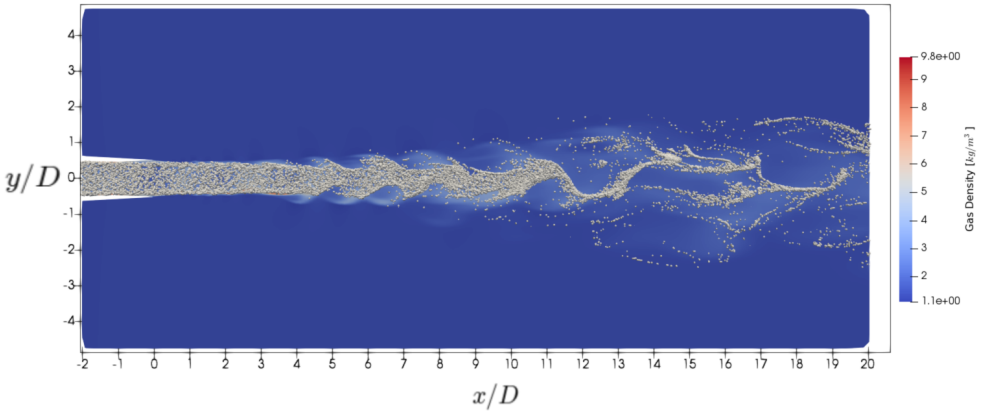

Fig. 6 Instantaneous density plot of two-phase jet flow at the $x-y$ plane.

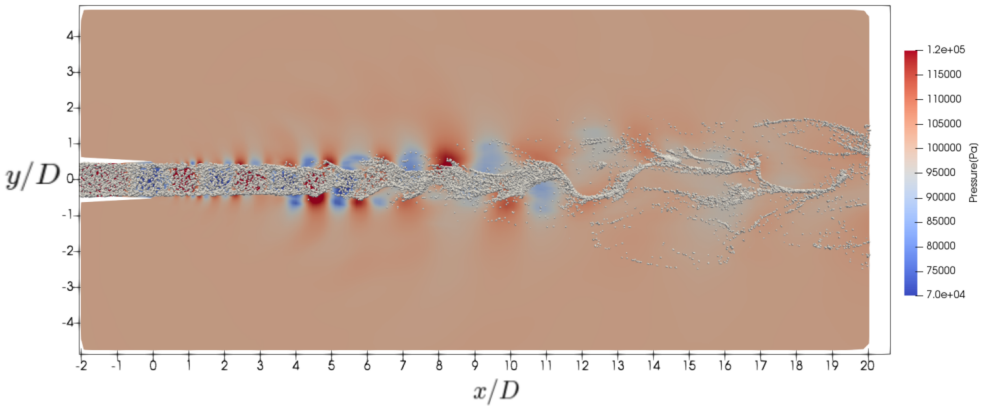

Fig. 7 Instantaneous pressure plot of two-phase jet flow at the $x-y$ plane.

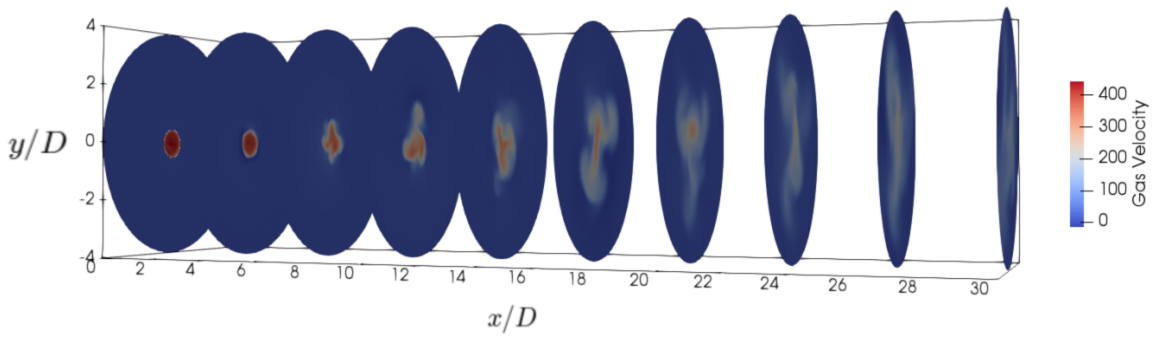

Fig. 8 Contour plot of gas velocity of the particle-laden jet.

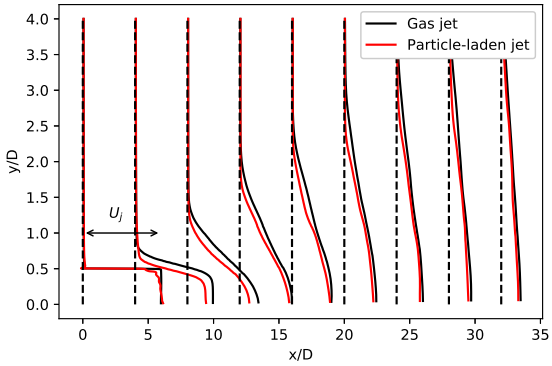

Fig. 9 Velocity profiles in the radial direction.

Figures 6 and 7 show the instantaneous density and pressure contour of the two-phase jet flow with the same NPR as the air jet. The flow properties are shown on the $x-y$ plane, and the particles are represented as solid spheres if they are located on or within a short distance of the $x-y$ plane. Compared to Figs. 3 and 4, the turbulent structures in the two-phase jet are more pronounced. The pattern of alternating high to low pressure in the shear region remains further downstream. Furthermore, although being injected uniformly in space at the nozzle inlet, the particles accumulate toward the nozzle wall where the flow velocity is lower. This is observed also by Balachandar [53]. In the plume, the particles develop a saddle shape that roughly corresponds to the large-scale turbulent structures. Figure 8 shows the instantaneous contour plots of gas velocity in consecutive cross-sections located $3D$ apart along the centerline of the nozzle in the particle-laden jet. Shear layer growth is clearly observed from contour at $x = 3D$ to $x = 6D$, where the gas velocity in the shear layer decreases due to turbulent mixing and particle-gas interaction. The shear layer continues to grow and develops azimuthal structures further downstream, then becomes fully turbulent aft of the potential core.

Figure 9 shows the comparison of the time-averaged streamwise velocity profiles of the gas and particle-laden jets. The streamwise velocities are normalized with fully expanded jet velocity, U_j. In both cases, the initial shear layer starts to grow downstream of the nozzle lip. However, noticeable differences in profile shape are observed at the nozzle exit, where the mean velocity within the plume is not uniform for the particle-laden jet. The particles within the nozzle are not distributed uniformly. More specifically, they accumulate and form clusters toward the nozzle wall, where the streamwise velocity is lower. This is believed to cause the local radial velocity gradient. In the potential core, namely $x/D < 8$, the shear layer is thinner for the particle-laden jet than that of the gas jet, and the mean velocity within the plume decreases significantly, by approximately 15%, from the exit velocity in the particle-laden jet. Moreover, the shear layer growth is considerably slower with particles in the jet, as shown by the velocity deficit up to $25D$.

Figure 10 shows the comparison of normalized mean gas velocity and particle velocity on the nozzle centerline. The particles and gas phase are in equilibrium in terms of velocity at the nozzle inlet, where the particles are released. The

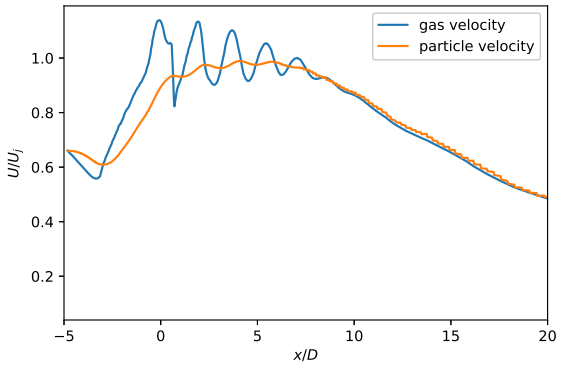

Fig. 10 Mean particle streamwise velocity on the nozzle centerline.

velocity of both phases decrease in a small region in the nozzle downstream of the inlet. In this region, the particle velocity is larger than the gas velocity. Further downstream within the nozzle, the gas expands and accelerates. In this region, although the particles also accelerate because of the drag force applied by the gas, their velocity is lower than the gas velocity. The particle velocity is approximately 0.9 U_j at the nozzle exit, where the gas velocity is much higher, at 1.1 U_j. Aft of the nozzle exit, alternating shock and expansion waves occur due to the difference of gas pressure and nozzle back pressure. The gas velocity fluctuates between 1.1 U_j and 0.8 U_j from nozzle exit to 8D downstream. The mean particle velocity in the potential core also decreases downstream relative to the shock waves, and increases downstream of expansion wave, but the acceleration of the particles are much lower. This shows the relaxation process the particles undergo when passing a shock or expansion wave. The velocity of the particles also gradually increases after going through each shock-cell in the potential core until 10D from the nozzle exit, where gas and particle velocities matches again. Beyond 10D from the nozzle exit, velocities of both the gas and particles decreases in the streamwise direction at comparable rates.

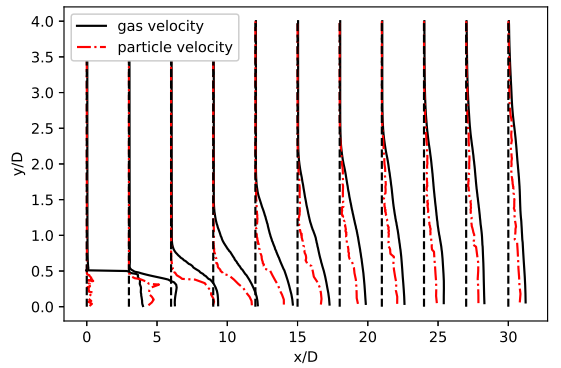

Fig. 11 Mean gas and particle velocity profiles on the radial direction.

Velocity profiles of gas and particles in the radial direction are shown in Fig. 11. The particle velocity profiles from x/D from 0 to 10 show that the mean velocity of the particle outside the shear layer are negligible. Particle velocities are negligibly small in the region where the radial distance is greater than 0.5D and axial distance is less than 10D from the nozzle exit plane center. This shows that particles are mostly contained in the potential core and rarely escape the region. Further downstream, velocity of particles from 0.5D to 1D in the radial direction begin to increase, due to the growth of the shear layer. However, the particle velocity is lower than the gas velocity at the same radial location.

Figure 12 shows the comparison of TKE with the RANS simulation using FUN3D. The TKE are sampled along the nozzle centerline (Fig. 12a) and the lipline (Fig. 12b). The streamwise location of the peak value of the TKE on the nozzle lipline coincides with the RANS results, but the peak value of our simulation is 10% higher, which is to be

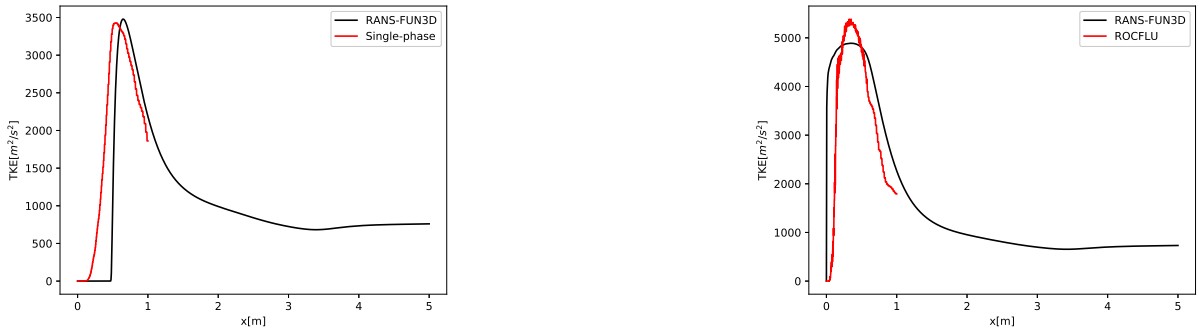

(a) Nozzle centerline. **(b) Nozzle Lipline.**

Fig. 12 Comparison of turbulent kinetic energy.

expected as the peak is more accurately captured via LES. The TKE on the nozzle centerline also agrees with the RANS results, except that FUN3D predicts no TKE up to $10D$, which is not physical as measurements show measurable TKE present within the core.

Aeroacoustics of the Particle-Laden Jet

Figure 13 shows the comparison of far-field SPL spectra of the gas jet and the particles-laden jet at radiation angle of 160° in the upstream axis. In this direction, the large-scale turbulent mixing noise is the most dominant noise component, and the overall SPL is the largest. In both the gas and the particle-laden jet, the peak noise frequency is approximately St of 0.2, which is typically the frequency of Mach wave radiation. This shows that the large-scale turbulent mixing noise, especially Mach wave radiation, dominates the noise radiated downstream, in both gas and particle-laden jets. However, the large-scale turbulent mixing noise is less intensive in the particle-laden jet. Reduced SPL from St of 0.01 to 0.4 is observed in the particle-laden jet. The SPL reduction is also observed by Buchta et al. [40] in supersonic free-shear flow with particles.

Figure 14 shows the ΔdB difference in SPL spectra of the particle-laden jet. Over 5 dB noise reduction is found in the low frequency components with St below 0.8, and the spectra show no significant difference with St beyond 1.0. The largest SPL difference is found at St of 0.04, where the SPL of the particle-laden jet is over 15dB lower than the gas jet.

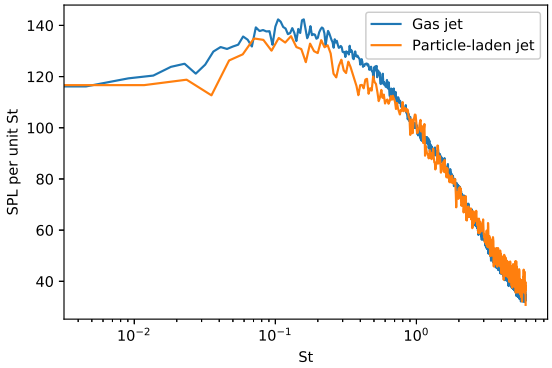

Fig. 13 Sound pressure level spectral at radiation angle of 160 degree.

Alteration of the Quadrupole Sources

We investigate the sound source of single and two-phase jets using Lighthill's acoustic analogy and Goldstein's generalized acoustic analogy [55]. Figure 15 shows the statistics of the first component, $\mathcal{T}_{11}$, of Lighthill's stress tensor

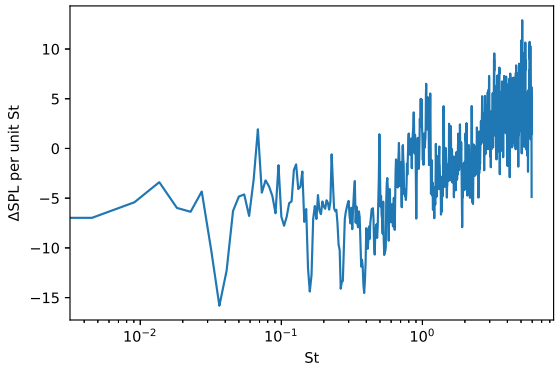

Fig. 14 ΔdB difference in Sound pressure level spectral of gas jet and particle-laden jet at radiation angle of 160 degree.

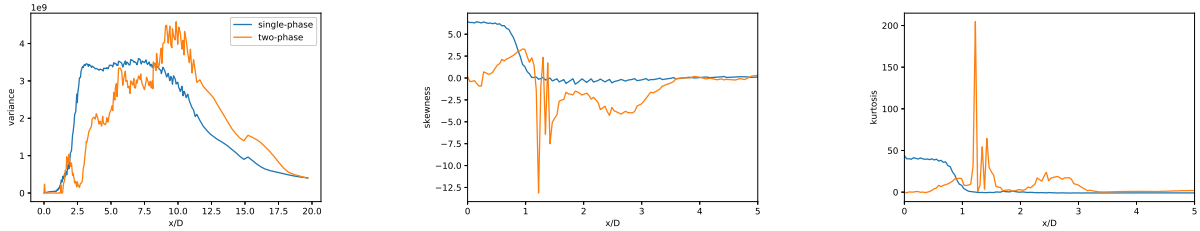

(a) Variance **(b) Skewness** **(c) Kurtosis**

Fig. 15 Statistics of $\mathcal{T}_{11}$ of Lighthill's stress tensor.

on the nozzle lipline starting from $x = 0$, $y = D/2$, and $z = 0$. The highest variance of two-phase jet flow is found at $x = 10D$, which is just downstream of the end of the potential core (see Fig. 5). Both Figs. 15b and 15c show that the source distribution from $x/D = 1$ to 1.5 are highly negatively skewed. They show a strong correlation from the presence of solid particles relative to the sound generation. Figure 16 shows the two-point cross-correlation of a point located at $x = D$, $y = D/2$, and $z = 0$ to all other points along the lipline in the axial direction. The correlation does not change with particles in the limited region, around $0.1D$, from the base point. The two-phase jet flow gradually become de-correlated outside the $0.1D$ region. The oscillation of the correlation coefficient from 0.5 to $1.5D$ of the air jet flow is not observed in the two-phase jet. This implies that the sound source in the two-phase jet is more compact than that of the air jet.

Figure 17 shows the contour plot of magnitude of $\mathcal{T}_{11}$ of Lighthill's stress tensor in space and time for the gas jet (Fig. 17a) and the particle-laden jet (Fig. 17b). The source strength in the gas jet is larger before the potential core ends at around $8D$, and the source strength is orders of magnitude smaller with $x/D > 15$. This is consistent with that of a larger coherent turbulent structure, which is more likely found in the shear layer than the region where flow becomes fully turbulent. Moreover, we predict that the source moves at a convection velocity close to Mach 1.0. This agrees with the observation that the turbulent eddies convect at around 0.6 U_j in the turbulent shear layers. The source strengths are dramatically different in the particle-jet. More specifically, the strength in the potential core region is much lower, and the coherent structures of the quadrupole sources exist beyond $10D$ downstream of the nozzle exit, which is roughly where the potential core ends. In addition, the convection velocity is slightly lower than the gas jet, at around 0.9 Mach from 0 to $5D$, but the velocity increases from 5 to $10D$ to nearly the ambient speed of sound, c_∞.

Figures 18 and 19 show the contour plots of the strength of $\mathcal{T}_{11}$ of the Lighthill's stress tensor in the freqency-wavenumber space of gas and particle-laden jets, respectively. These plots indicate the phase velocity, ω/k, of the sound sources. By comparison, the sound sources in the gas jet have a larger phase velocity than that of the particle-laden jet. The phase velocities of both jets are lower than the convection velocity. This shows that the convection velocity decreases in the downstream direction. In addition, a large portion of the sound sources in the particle-laden jet are

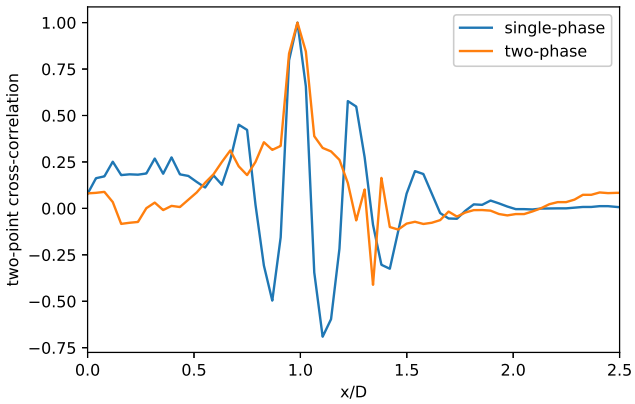

Fig. 16 Two-point cross-correlation of $\mathcal{T}_{11}$ of Lighthill's stress tensor.

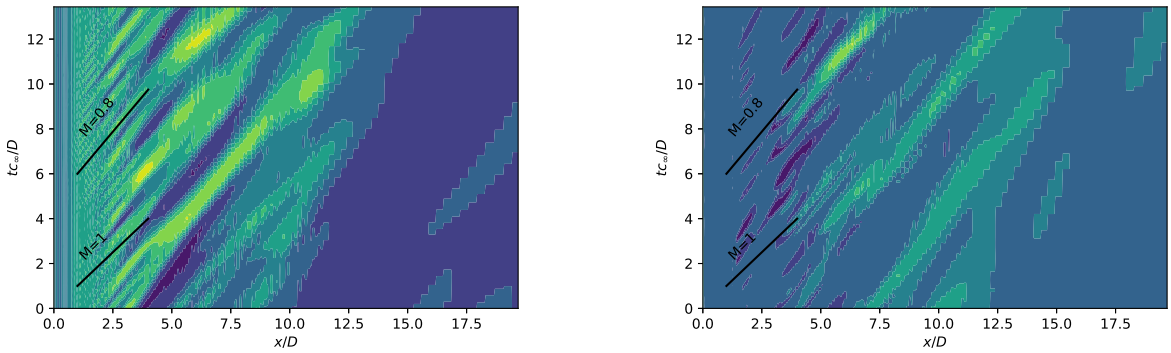

(a) Gas jet. **(b) Particle-laden jet.**

Fig. 17 Contour plot of $\mathcal{T}_{11}$ of Lighthill's stress tensor on the lip-line, with respect to streamwise location and time.

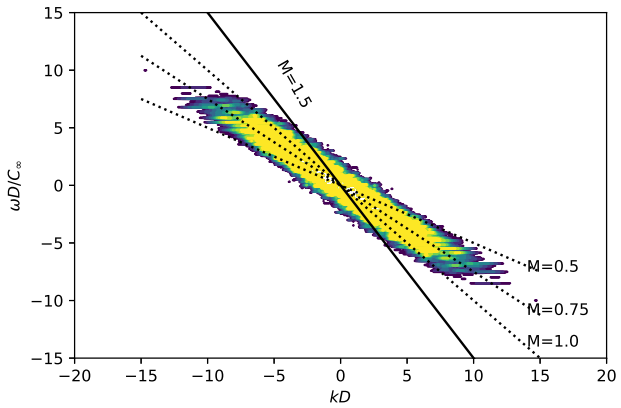

Fig. 18 Contour plot of $\mathcal{T}_{11}$ of the Lighthill's stress tensor of the gas jet in frequency and wave number space.

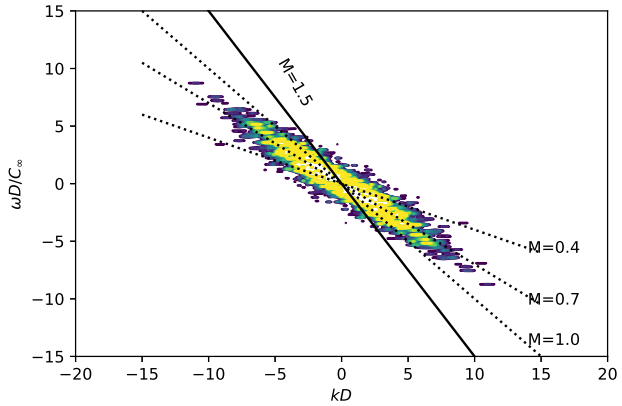

Fig. 19 Contour plot of $\mathcal{T}_{11}$ of the Lighthill's stress tensor of the particle-laden jet in frequency and wave number space.

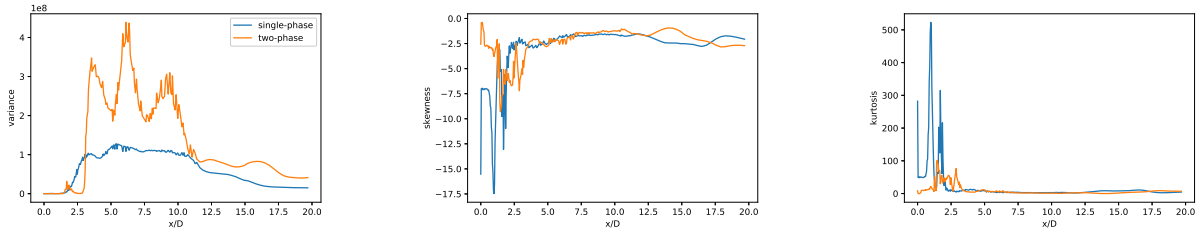

(a) Variance **(b) Skewness** **(c) Kurtosis**

Fig. 20 Statistics of $\mathcal{G}_{11}$ of Goldstein's equivalent source.

subsonic, in the range of $0.4 < M < 1.0$.

Figure 20 shows the variance, skewness, and kurtosis of the first component of Goldstein's equivalent source. Here, we choose the non-parallel mean flow as the base flow. According to Goldstein [55], the sound source, in this case, is the generalized Reynold's stress, $\mathcal{G}_{ij} =< \rho V_i V_j - \bar{\rho}\bar{V}_i\bar{V}_j >$. By using this formulation, the refraction is accounted for by the left hand side of the equation, hence it is no longer a part of the source term. In terms of the statistics of the source, the variance within the core region is drastically different between single and two-phase jets, and the skewness and kurtosis are only significantly different up to $4D$. The variance of the two-phase flow is much larger than that of single-phase flow at the streamwise locations from $2.5D$ to $10D$. It shows that the sound source of two-phase flow deviates more from the mean than that of the single phase flow.

Figure 21 shows the two-point cross-correlation of G_{11} of Goldstein's equivalent source on the nozzle lipline. The differences of the two correlation curves are not significant, but the sound source of two-phase jets spans a slightly longer distance downstream, approximately $0.1D$.

Sound Generated by the Effect of Particulates

We compute the monopole and dipole sources on the nozzle lipline according to Crighton and Ffowcs William's [61] acoustic analogy for two-phase flow. Figure 22 shows the mean monopole source and three components of the mean dipole sources located on the nozzle lip-line. The magnitude of the overall monopole sources are larger than the streamwise component dipole sources, except in a small region near $x/D = 10$, where the dipole sources reach a local maximum value of 20. The turbulent mixing intensifies in this region and the drag forces applied on the particles also are maximum here. Figures 10 and 11 also indicate that particles in this region start to decrease in velocity due to the growth of the shear layer and the mixing of low velocity gas. By comparison, the magnitude of both the monopole and dipole sources are much less than the magnitude of the Lighthill's stress tensor, $\mathcal{T}_{ij}$.

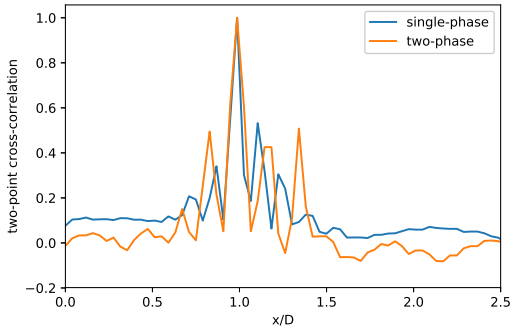

Fig. 21 Two-point cross-correlation of $\mathcal{G}_{11}$ of Goldstein's equivalent source.

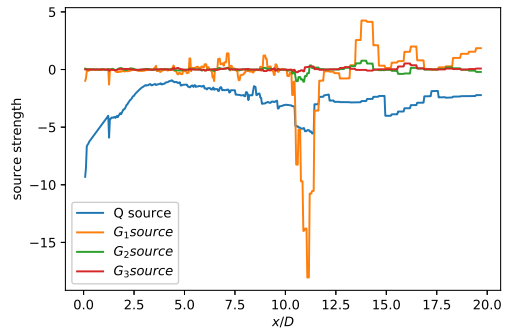

Fig. 22 Mean strength of the monopole and dipole sound sources located on the nozzle lipline.

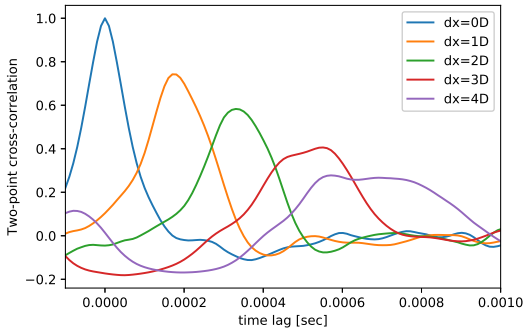

Fig. 23 Two-point cross-correlation curves of the monopole source on the nozzle lipline. Reference point: $x = 10D$.

Figure 23 shows the two-point cross-correlation curves of the monopole sources on the nozzle lip-line. The reference point is located $10D$ from the nozzle exit, where the source strength is high, and other points are located $0D$ to $4D$ from the reference point. The monopole sources show a correlation coefficient of 0.5 or more over the span of $3D$ in the streamwise direction. This indicates a strong coherent motion of the monopole sound sources; however, the convection velocity of the source is subsonic compared to the ambient sound speed. Thus, the sound sources are inefficient in radiating sound to the far-field.

Figure 24 shows the two-point correlation curve of the streamwise component of the dipole sources on the nozzle lip-line. Since the dipole source consists of force applied by the particles on the gas and the time rate change of

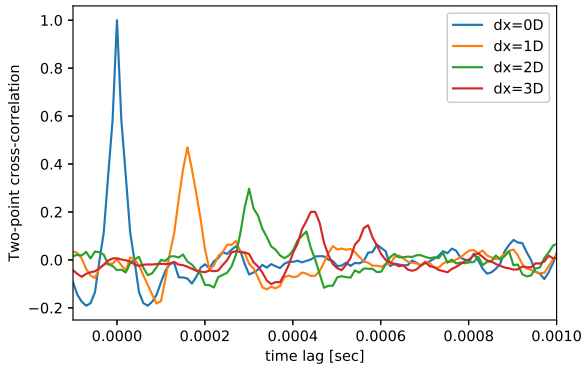

Fig. 24 Two-point cross-correlation curves of the streamwise component of the dipole source on the nozzle lipline. Reference point: $x = 10D$**.**

momentum due to the particles, it is no surprise that the sources convect at velocity of the particles. In addition, the dipole sources are very compact in space, at the length-scale of the particles' diameters. This is shown by the auto-correlation curve ($dx = 0D$ curve in Fig. 23), which decrease rapidly to zero correlation in less than 1×10^{-4} s.

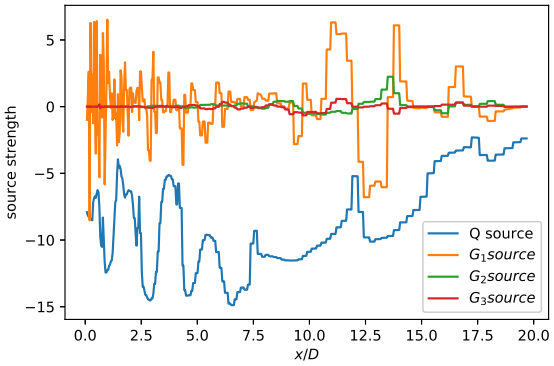

Fig. 25 Mean strength of the monopole and dipole sound sources located on the nozzle centerline.

Figure 25 shows the mean source strength of particle-induced sound sources on the nozzle centerline. Compared to the shear layer, the volume fractions of the particles are greater; therefore, the monopole sources due to the volume of the particles are dominated over the dipole sources. It is consistent with the particle velocities, which do not differ from the surrounding air by a significant amount (shown in Fig. 10), especially at larger downstream locations. Figures 26 and 27 show the two-point cross-correlations with the reference point located on the nozzle centerline and $10D$ downstream from the nozzle exit. Both sources show a low level of correlation on the centerline. The correlation coefficients drop below 0.3 within $2D$ from the reference point.

IV. Summary and Future Work

In this study, we describe the numerical approach we created to analyze the far-field noise radiated from high-speed single-phase and two-phase gas-particle jet flows. The numerical investigation involves compressible CFD simulations of the gas jet and particle-laden jet, and the evaluation of FWH equation on permeable surfaces within the near-field of the flow. Far-field noise is directly computed using a modified Farrasat's formulation [60]. The acoustic spectra are dominated by large-scale turbulent mixing noise in the downstream radiation direction. The predication of large-scale structures are validated with the SHJAR database. More importantly, the acoustic spectra from the gas jet and particle-laden jet are compared, and drastic differences are predicted between them. Equivalent sources of Lighthill's

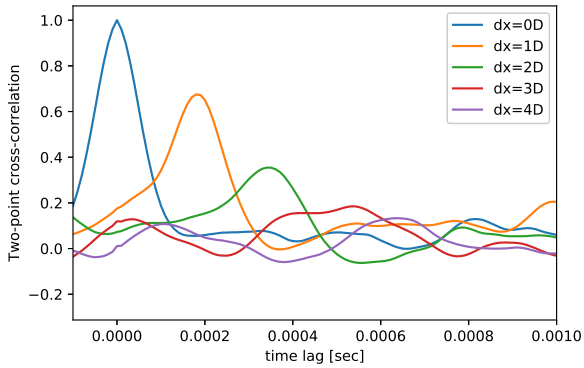

Fig. 26 Two-point cross-correlation curves of the monopole source on the nozzle centerline. Reference point: $x = 10D$**.**

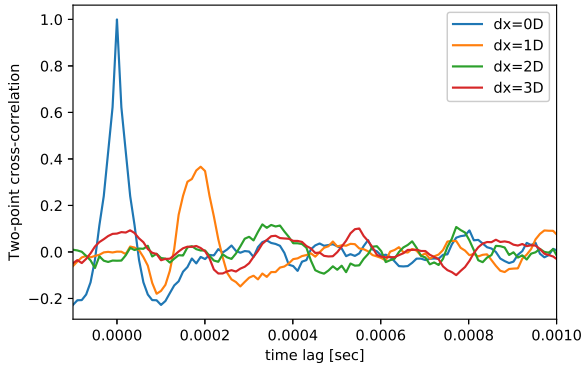

Fig. 27 Two-point cross-correlation curves of the streamwise component of the dipole source on the nozzle centerline. Reference point: $x = 10D$**.**

and Goldstein's acoustic analogies are evaluated for both single and two-phase flows. The location, convective velocity, and phase speed of the equivalent sources are compared. Observation of the sources shows that their location are greatly altered, and both the convection and phase velocity of the particle-laden jet are lower than the gas jet. Moreover, the correlation coefficient on the nozzle lipline are compared. We show that the correlation of Lighthill's stress tensor shows dramatic differences with and without particles in the flow, while the correlation of Goldstein's equivalent sources are much more similar.

Two additional sound sources in the particle-laden jet, the monopole and dipole sources, due to the presence of particles, are evaluated. We find that these two sources are directly related to the particles volume fraction and aerodynamic force applied by the particles to the gas. However, the strength of these two sources are much smaller relative to the Lighthill stress tensor. In addition, the time-lagged two-point cross-correlation are computed for both sources. They reveal that the monopole sources are more correlated than the dipole sources, and the dipoles sources are very compact in space.

The next step of this study includes developing a volumetric integration method using Crighton and Ffowcs William's acoustic analogy [61] to evaluate the spectral components of the monopole and dipole sources in the particle-laden jets. We will directly evaluate the impact of particulates on the large-scale mixing noise that is essential for causing vibro-acoustic loading on the flight vehicle. The study of the noise generation process of high-speed two-phase flow will contribute to the development of a new reduction method of launch noise and alleviate the damage caused by solid rocket engines.

Acknowledgements

This research is supported by the Space Research Initiative (SRI) OR-DRPD-SRI2019: Prediction and Reduction of Noise from Rockets to Eliminate Failure and Fatigue, the University of Florida Department of Mechanical and Aerospace Engineering, and the Herbert Wertheim College of Engineering.

References

[1] Davenas, A., *Solid Rocket Propulsion Technology*, Pergamon Press, 1993. doi:10.1016/c2009-0-14818-3.

[2] Dash, S. M., Wolf, D. E., Beddini, R. A., and Pergament, H. S., "Analysis of Two-phase Flow Processes in Rocket Exhaust Plumes," *Journal of Spacecraft and Rockets*, Vol. 22, No. 3, 1985, pp. 367–380. doi:10.2514/3.25758.

[3] Hess, R. W., Fralich, R. W., and Hubbard, H. H. a., "Studies of Structural Failure Due to Acoustic Loading," *NACA-TN-4050*, 1957.

[4] "Study of Solid Rocket Motor for a Space Shuttle Booster," NASA-CR-123687, March 1972.

[5] Hale, M. E., "The Development of Advanced Launch System Noise Criteria for Future Space Port Site Selection," *Proceedings Inter-Noise 89*, 1989.

[6] McInerny, S. A., "Launch Vehicle Acoustics. I - Overall Levels and Spectral Characteristics," *Journal of Aircraft*, Vol. 33, No. 3, 1996, pp. 511–517. doi:10.2514/3.46974.

[7] McInerny, S., "Rocket Noise – A Review," *13th Aeroacoustics Conference, AIAA Paper 90-3981*, 1990. doi:10.2514/6.1990-3981.

[8] Bourgine, A., and Dordain, J., "Review of Acoustic Studies Carried Out at ONERA in the Field of Space Vehicles," *Journal of the British Interplanetary Society*, Vol. 34, 1981, pp. 72–80.

[9] Humphrey, A. J., "Rocket Noise Environments," *Dept. of Defense - Shock and Vibration Bulletin*, 1957, pp. 10–17.

[10] Regier, A. A., Mayes, W. H., and Edge, P. M., "Noise Problems Associated with Launching Large Space Vehicles," *Sound: Its uses and Control*, Vol. 1, No. 6, 1962, pp. 7–12. doi:10.1121/1.2369585.

[11] Cole, J. N., Eldred, K. M., Humphrey, A. J., Kyrazis, D. T., and Von Kierke, H. E., "Noise Radiation from Fourteen Types of Rockets in the 1,000 to 130,000 Pounds Thrust Range," *Aerospace Medical Div. Aerospace Medical Research Labs, WADC-TR-57-354*, 1957.

[12] Cole, J. N., England, R. T., and Powell, R. G., "Effects of Various Exhaust Blast Deflectors on the Acoustic Noise Characteristics of 1000 Pound Thrust Rockets," *Wright Air Development Division, WADD TR 60-6*, 1960.

[13] Cole, J. N., and Thomas, C. E., "Far Field Noise and Vibration Levels Produced During the Saturn SA-1 Launch," *United States Air Force, ASD TR 61-607*, 1961.

[14] Cole, J. N., Powell, R. G., and Hille, H. K., "Acoustic Noise and Vibration Studies at Cape Canaveral Missile Test Annex, Atlantic Missile Range," *Armed Services Technical Information Agency, Technical Report 61-608 (I)*, Vol. 1, 1962.

[15] Sutherland, L. C., "Preliminary Acoustic and Vibration Environment. Saturn S-IB," *Boeing Technical Report D2-12955*, 1961.

[16] Tedrick, R. N., and Thornton, C. C., "Results of the Far Field Acoustical Survey of the SA-4 Launch," *NASA TM-X-51348*, 1963.

[17] Tedrick, R. N., "Far-field Acoustic Levels Resulting from Titan Launches," *NASA-TM-X-54632*, 1962.

[18] Alestra, S., Terrasse, I., and Troclet, B., "Inverse Method for Identification of Acoustic Sources at Launch Vehicle Liftoff," *AIAA Journal*, Vol. 41, No. 10, 2003, pp. 1980–1987. doi:10.2514/2.7318.

[19] Panda, J., Mosher, R. N., and Porter, B. J., "Noise Source Identification During Rocket Engine Test Firings and a Rocket Launch," *Journal of Spacecraft and Rockets*, 2014, pp. 1–12. doi:10.2514/1.A32863.

[20] Lassiter, L. W., and Heikotter, R. H., "Some Measurements of Noise from Three Solid-Fuel Rocket Engines," *NACA-TN-3316*, 1954.

[21] Mull, H. R., and Erickson, J. C., "Survey of the Acoustic Near Field of Three Nozzles at a Pressure Ratio of 30," *NACA-TN-3978*, 1957.

[22] Mayes, W. H., Lanford, W. E., and Hubbard, H. H., "Near-Field and Far-Field Noise Surveys of Solid-Fuel Rocket Engines for a Range of Nozzle Exit Pressures," *NASA TN D-21*, 1959.

[23] Tedrick, R. N., "Acoustical Measurements of Static Tests of Clustered and Single Nozzled Rocket Engines," *Journal of the Acoustical Society of America*, Vol. 36, No. 11, 1964, pp. 2027–2032. doi:10.1121/1.1919318.

[24] Foulon, H., Gely, D., Varnier, J., Zoppellari, E., and Marchesse, Y., "MARTEL Facility: Simulation of Space Launchers Aeroacoustic Ambiance," *ONERA TP 2000-7*, 2000.

[25] Fukuda, K., Tsutsumi, S., Fujii, K., Ui, K., Ishii, T., Oinuma, H., Kazawa, J., and Minesugi, K., "Acoustic Measurement and Prediction of Solid Rockets in Static Firing Tests," *15th AIAA/CEAS Aeroacoustics Conference, AIAA Paper 2009-3368*, 2009. doi:10.2514/6.2009-3368.

[26] Horne, W., Burnside, N., Panda, J., and Brodell, C., "Measurements of Unsteady Pressures near the Plume of a Solid Rocket Motor," *15th AIAA/CEAS Aeroacoustics Conference, AIAA Paper 2009-3323*, 2009. doi:10.2514/6.2009-3323.

[27] Panda, J., and Mosher, R., "Use of a Microphone Phased Array to Determine Noise Sources in Rocket Plumes," *49th AIAA Aerospace Sciences Meeting, AIAA Paper 2011-974*, 2011. doi:10.2514/6.2011-974.

[28] Panda, J., and Mosher, R., "Identification of Noise Sources in a Model Scale Lift-Off Test using a Microphone Phased Array," *50th AIAA Aerospace Sciences Meeting*, 2012. doi:10.2514/6.2012-1171.

[29] Panda, J., and Mosher, R., "Microphone Phased Array to Identify Liftoff Noise Sources in Model-Scale Tests," *Journal of Spacecraft and Rockets*, Vol. 50, No. 5, 2013, pp. 1002–1012. doi:10.2514/1.A32433.

[30] Gely, D., Elias, G., Mascanzoni, F., and Floulon, H., "Acoustic Environment of the VEGA Launch Vehicle at Lift-Off," *Forum Acusticum*, 2005.

[31] Casalino, D., Santini, S., Genito, M., and Ferrara, V., "Rocket Noise Sources Localization Through a Tailored Beam-Forming Technique," *AIAA Journal*, Vol. 50, No. 10, 2012, pp. 2146–2158. doi:10.2514/1.J051479.

[32] Moran, R. P., and Houston, J. D., "Infrared Imagery of Solid Rocket Exhaust Plumes," *JANNAF 6th Liquid Propulsion Subcommittee Meeting*, 2011. doi:10.2514/6.2013-2448.

[33] Panda, J., James, G., Brunside, N., Fong, R., Fogt, V., and Ross, J., "Use of Heated Helium to Simulate Surface Pressure Fluctuations on the Launch Abort Vehicle During Abort Motor Firing," *17th AIAA/CEAS Aeroacoustics Conference, AIAA Paper 2011-2901*, 2011. doi:10.2514/6.2011-2901.

[34] Panda, J., Burnside, N. J., Fong, R. K., Ross, J. C., James, G. H., and Fogt, V. A., "Heated Helium to Simulate Surface Pressure Fluctuations Created by Rocket Motor Plumes," *AIAA Journal*, Vol. 51, 2013, pp. 302–314. doi:10.2514/1.J051485.

[35] Kiris, C. C., Barad, M. F., Housman, J. A., Sozer, E., Brehm, C., and Moini-Yekta, S., "The LAVA Computational Fluid Dynamics Solver," *52nd AIAA Aerospace Sciences Meeting, AIAA Paper 2014-0070*, 2014. doi:10.2514/6.2014-0070.

[36] Putnam, G. C., and Strutzenburg, L. L., "Simulation of Acoustics for Ares I Scale Model Acoustic Tests," *Journal of the Acoustical Society of America*, Vol. 130, No. 2543, 2011. doi:10.1121/1.3655163.

[37] Putnam, G. C., "Simulation of Ares Scale Model Acoustic Test Overpressure Transients Using Computational Fluid Dynamics," *Acoustical Society of America Meeting, Paper M11-1226*, 2011.

[38] Putnam, G., "Simulations of Rainbird Water Spray with Lagrangian Particles Using Loci/CHEM," *Jacobs ESTS Group Report ESTSG-FY10-02643*, 2010.

[39] Putnam, G., "Constellation: Simulation of Solid Rocket Booster Hole Water Deluge with Lagrangian Particles Using Loci/CHEM," *NASA/MSFC Technical Report ESTSG-FY10-02529*, 2010.

[40] Buchta, D. A., Shallcross, G., and Capecelatro, J., "Sound and turbulence modulation by particles in high-speed shear flows," *Journal of Fluid Mechanics*, Vol. 875, 2019, pp. 254–285. doi:10.1017/jfm.2019.467, URL `https://doi.org/10.1017/jfm.2019.467`.

[41] Chobotov, V., and Powell, A., "On the Prediction of Acoustic Environments from Rockets," *The Ramo-Wooldridge Corporation GM-TR-190*, 1957.

[42] Franken, P. A., "Methods of Space Vehicle Noise Prediction," *WADC Technical Report 58-343*, 1960.

[43] Morgan, W. V., Sutherland, L. C., and Young, K. J., "The Use of Acoustic Scale Models for Investigating Near Field Noise of Jet and Rocket Engines," *WADD Technical Report 61-178*, 1961.

[44] Wilhold, G. A., Guest, S. H., and Jones, J. H., "A Technique for Predicting Far-Field Acoustic Environments Due to a Moving Rocket Sound Source," 1963.

[45] Crocker, M. J., and Potter, R. C., "Acoustic Prediction Methods for Rocket Engines, Including the Effects of Clustered Engines and Deflected Exhaust Flow," *NASA CR-566*, 1966.

[46] Eldred, K. L., "Acoustic Loads Generated by the Propulsion System," *NASA-SP-8072*, 1971.

[47] Candel, S., "Analysis of the Sound Field Radiated by the Ariane Launch Vehicle During Lift-Off," *La Rech. Aerospatiale*, Vol. 6, No. 217, 1984, pp. 17–33.

[48] Casalino, D., Barbarino, M., Genito, M., and Ferrara, V., "Hybrid Empirical/Computational Aeroacoustics Methodology for Rocket Noise Modeling," *AIAA Journal*, Vol. 47, No. 6, 2009, pp. 1445–1460. doi:10.2514/1.38634.

[49] Counter, D. D., and Houston, J., "Verification of Ares I Liftoff Acoustic Environments via the Ares I Scale Model Acoustic Test," *27th Aerospace Testing Seminar*, 2012.

[50] Gely, D., Elias, G., Bresson, C., Foulon, H., and Radulovic, S., "Reduction of Supersonic Jet Noise - Application to the Ariane 5 Launch Vehicle," *6th Aeroacoustics Conference and Exhibit, AIAA Paper 2000-2026*, 2000. doi:10.2514/6.2000-2026.

[51] Ignatius, J. K., Sankaran, S., Kumar, R. A., and Satyanarayana, T. N. V., "Suppression of Jet Noise by Staged Water Injection During Launch Vehicle Lift-Off," *International Journal of Aeroacoustics*, Vol. 7, No. 3-4, 2008, pp. 223–241. doi:10.1260/1475-472X.7.3.223.

[52] Kuo, K. K. (ed.), *Fundamentals of Solid-Propellant Combustion*, American Institute of Aeronautics and Astronautics, 1984. doi:10.2514/4.865671.

[53] Balachandar, S., and Eaton, J. K., "Turbulent Dispersed Multiphase Flow," *Annual Review of Fluid Mechanics*, Vol. 42, No. 1, 2010, pp. 111–133. doi:10.1146/annurev.fluid.010908.165243.

[54] Lighthill, M. J., "On Sound Generated Aerodynamically. I. General Theory," *Proceedings of the Royal Society A: Mathematical, Physical and Engineering Sciences*, Vol. 211, No. 1107, 1952, pp. 564–587. doi:10.1098/rspa.1952.0060.

[55] Goldstein, M. E., "A Generalized Acoustic Analogy," *Journal of Fluid Mechanics*, Vol. 488, 2003, pp. 315–333. doi:10.1017/s0022112003004890.

[56] Crowe, C. T., Schwarzkopf, J. D., Sommerfeld, M., and Tsuji, Y., *Multiphase Flows with Droplets and Particles*, CRC Press, 2011. doi:10.1201/b11103.

[57] Naumann, Z., and Schiller, L., "A Drag Coefficient Correlation," *Z. Ver Deutsch. Ing*, Vol. 77, 1935, pp. 318–323.

[58] Ranz, W., Marshall, W. R., et al., "Evaporation from Drops," *Chemical Engineering Progress*, Vol. 48, No. 3, 1952, pp. 141–146.

[59] Ffowcs Williams, J. E., and Hawkings, D. L., "Sound Generation by Turbulence and Surfaces in Arbitrary Motion," *Philosophical Transactions of the Royal Society of London A: Mathematical, Physical and Engineering Sciences*, Vol. 264, No. 1151, 1969, pp. 321–342. doi:10.1098/rsta.1969.0031.

[60] Farassat, F., "Derivation of Formulations 1 and 1A of Farassat," NASA/TM-2007-214853, 2007.

[61] Crighton, D., and Ffowcs Williams, J., "Sound generation by turbulent two-phase flow," *Journal of Fluid Mechanics*, Vol. 36, No. 3, 1969, pp. 585–603.

[62] Bridges, J., and Brown, C., "Validation of the Small Hot Jet Acoustic Rig for Aeroacoustic Research," *11th AIAA/CEAS Aeroacoustics Conference*, AIAA paper 2005-2846, 2005. doi:10.2514/6.2005-2846.

[63] Lau, J. C., Morris, P. J., and Fisher, M. J., "Measurements in Subsonic and Supersonic Free Jets Using a Laser Velocimeter," *Journal of Fluid Mechanics*, Vol. 93, No. 1, 1979, p. 1–27. doi:10.1017/S0022112079001750.